

RECURSIVE ESTIMATION OF NON-GRAVITATIONAL PERTURBATIONS FROM SATELLITE OBSERVATIONS

Lamberto Dell'Elce,

Ohad Ben-Yaacov, Pini Gurfil

University of Liège

Technion – Israel Institute of Technology

ABSTRACT

Third-body and gravitational perturbations can be modeled with sufficient precision for most applications in low-Earth orbit. However, owing to severe uncertainty sources and modeling limitations, computational models of satellite aerodynamics and solar radiation pressure are bound to be biased. Aiming at orbital propagation consistent with observed satellite orbital dynamics, real-time estimation of these perturbations is desired. The particle evolution is carried out by means of an underlying orbital propagator, and the Bayes rule is used to recursively update weights by comparing propagated orbital elements with satellite observations. The proposed formulation uses mean orbital elements as the only available measurements. This feature makes the algorithm a potentially-valuable resource for space situational awareness applications, such as space debris trajectories prediction from two-line elements, or for on-board force estimation from GPS data. High-fidelity simulations show that non-gravitational perturbations can be estimated with 20% accuracy.

Index Terms— Bayesian inference, particle filter, force estimation, drag, SRP

1. INTRODUCTION

To date, satellite drag and solar radiation pressure (SRP) estimation is mostly carried out by means of high-sensitivity accelerometers [1]. Nonetheless, force estimators using satellite observations only were also proposed. The method of dynamic model compensation (DMC) is arguably the most popular example of this class [2]: first, an underlying parametric model of the unknown perturbation is adopted; then, the parameters of the model are assumed to be first-order Gauss-Markov processes, and are appended to the state vector of a recursive estimator (most often an extended Kalman filter). Provided with sufficiently dense and accurate satellite observations, i.e., standard deviations of 5 m for the position and 1 mm/s for the velocity, DMC was successfully applied to the estimation of the atmospheric force [3]. However, no other process noise except the atmospheric force itself was considered in [3], so this result is arguably not representative of a real-life scenario. In [4], forces of the order of 10^{-3} N/kg were accurately estimated by means of DMC. Dense mea-

surements and analogous noise to [3] were considered. Similar accuracy was obtained when differentiation of global positioning system (GPS) data was implemented [5]. However, this accuracy is far from being sufficient to estimate drag or SRP which, in general, are 3 or more orders of magnitude smaller.

Batch estimators were used for ground-based estimation using observations [6]. In this case, measurement noise could be largely relaxed, e.g., two-line elements (TLE) were used in [7], but they were not suitable for recursive implementation. An alternative approach based on optimal control policies was recently developed in [8]. This technique was able to account for both atmospheric drag and SRP, and could be naturally extended to complex models of the force, but it is also unsuitable for recursive estimation.

In the broader context of Bayesian estimation of dynamical systems, sequential Monte Carlo (SMC) algorithms, which include particle filters, are valuable tools for optimally approximating the posterior distribution of hidden Markov processes [9, 10]. Compared to Kalman filtering techniques, particle filters do not require any assumption on neither the linearity of the system nor the nature of the noise. Such generality is obtained at the price of a greater computational burden. Particle filters were used in several problems in astrodynamics, e.g., space object tracking [11], orbit determination [12, 13], and relative state estimation [14, 15]. However, to the best of our knowledge, there has not been an attempt of non-gravitational force estimation using particle filters, which is available in the literature.

In this paper, we develop an SMC algorithm for the recursive inference of non-gravitational perturbations from satellite observations with no supporting in-situ acceleration measurements. Our approach is conceptually similar to DMC, but in addition to the aforementioned advantages and drawbacks of SMC, we show that the proposed algorithm provides good estimates of the non-gravitational perturbations even when fairly inaccurate measurements and a modest underlying propagator are used.

The filter developed herein works by updating the empirical distribution of a finite number of weighted particles. Each particle consists of one set of orbital elements and some parameters, e.g., drag and reflectivity coefficients, used to evaluate a prescribed parametric model for non-gravitational

forces. Particles are updated by means of an underlying orbital propagator, and are assigned weights based on the error between propagated orbital elements and satellite observations. Secular effects of the non-gravitational perturbations allow ‘good’ particles to emerge when weights are recursively updated.

Mean orbital elements are exploited as the only measurements. They can be obtained either by converting GPS states using a contact transformation or by using TLE. The first option is pursued in this paper. Such a transformation is undoubtedly a noise source, so that one may argue that direct GPS measurements should be used instead. Nonetheless, averaged elements have two compelling features: first, their dynamics exhibit robustness for mis-modeling of high-degree gravitational harmonics; second, they pave the way to the exploitation of computationally-efficient analytical and semi-analytical techniques, e.g., SGP4, to propagate particles.

The paper is organized as follows. Section 2 discusses the mathematical background on SMC and outlines the algorithm of the filter. Section 3 details the different ingredients of the problem of non-gravitational force estimation. Insight and caveats on the choice of the parameters of the filter are discussed as well. Finally, numerical simulations in a high-fidelity environment are carried out in Section 4.

2. SEQUENTIAL MONTE CARLO FOR PARAMETER AND STATE ESTIMATION

Let $\mathbf{P} \in \mathcal{I}_{\mathbf{P}}$ and $\{\mathbf{X}_{\tau} \in \mathcal{I}_{\mathbf{X}}, \tau \in \mathbb{N}^+\}$ be an $\mathcal{I}_{\mathbf{P}}$ -valued vector of uncertain parameters and an $\mathcal{I}_{\mathbf{X}}$ -valued discrete-time $(m+1)$ -th order Markov process indexed by non-negative integers, namely $\tau \in \mathbb{N}^+$, and provided with *transitional prior distribution*

$$\mathbf{X}_{\tau+1} | (\mathbf{x}_{\tau}, \mathbf{x}_{\tau-1}, \dots, \mathbf{x}_{\tau-m}, \mathbf{p}) \sim f(\mathbf{x}_{\tau+1} | \mathbf{x}_{\tau}, \dots, \mathbf{x}_{\tau-m}, \mathbf{p}) \quad \forall t \geq m \quad (1)$$

respectively; here, $f(\mathbf{x}_{\tau+1} | \mathbf{x}_{\tau}, \dots, \mathbf{x}_{\tau-m}, \mathbf{p})$ denotes the probability density function (PDF) defining how the process evolves given outcomes of the parameters’ vector and the past $m+1$ realizations of the state, i.e., $\mathbf{P} = \mathbf{p}$, $\mathbf{X}_{\tau-j} = \mathbf{x}_{\tau-j} \quad \forall j = 0, \dots, m$. Some $\mathcal{I}_{\mathbf{Y}}$ -valued observations, $\{Y_{\tau} \in \mathcal{I}_{\mathbf{Y}}, \tau \in \mathbb{N}^+\}$, conditionally independent in time, are available,

$$\mathbf{Y}_{\tau} | (\mathbf{x}_{\tau}, \dots, \mathbf{x}_0, \mathbf{p}) \sim g(\mathbf{y}_{\tau} | \mathbf{x}_{\tau}, \mathbf{p}) \quad \forall t \geq 0 \quad (2)$$

The PDF $g(\mathbf{y}_{\tau} | \mathbf{x}_{\tau}, \mathbf{p})$ is referred to as *marginal likelihood distribution*. Equations (1) and (2) define a hidden Markov model (HMM).

The filtering problem consists of estimating the *marginal posterior distribution* of the process, which is the joint PDF of \mathbf{P} and \mathbf{X}_{τ} conditional to the observations $\mathbf{Y}_0, \dots, \mathbf{Y}_{\tau}$ [10]:

$$\text{pdf}(\mathbf{x}_{\tau}, \mathbf{p} | \mathbf{y}_0, \dots, \mathbf{y}_{\tau}) \propto g(\mathbf{y}_{\tau} | \mathbf{x}_{\tau}, \mathbf{p}) \text{pdf}(\mathbf{x}_{\tau}, \mathbf{p} | \mathbf{y}_0, \dots, \mathbf{y}_{\tau-1}) \quad (3)$$

The analogy with Kalman filtering is established by considering f and g as non-linear and non-Gaussian generalizations of the predictor and innovation equations, respectively, and the marginal of the posterior distribution as the updated state and covariance estimates.

A closed-form solution of Eq. (3) is not generally available. Particle filters approximate the posterior by means of SMC sampling of Eq. (3). If direct sampling from $\text{pdf}(\mathbf{x}_{\tau}, \mathbf{p} | \mathbf{y}_0, \dots, \mathbf{y}_{\tau-1})$ is not possible or inconvenient, a proposal distribution, $q(\mathbf{x}_{\tau+1}, \mathbf{p} | \mathbf{y}_{\tau+1}, \mathbf{x}_{\tau}, \dots, \mathbf{x}_{\tau-m})$, is used, yielding the *importance sampling* approach. In theory, any PDF can be used as importance distribution, provided that its support covers $\mathcal{I}_{\mathbf{X}}$ and $\mathcal{I}_{\mathbf{P}}$. However, the adequate choice of the proposal distribution is crucial for achieving good performance of the filter and avoiding degeneracy [16].

Several SMC formulations exist [9, 10], but most of them do not consider parameter estimation. Our algorithm is mainly inspired by the work of Liu *et al.* [17], which combined state and parameter estimation by means of *artificial evolution* and *kernel smoothing* of parameters. The filter works by propagating a set of n particles from τ to $\tau+1$. Each particle consists of the last $m+1$ states, a set of parameters, and a weight:

$$j\text{-th particle} := \left\{ \mathbf{x}_{\tau}^{(j)}, \dots, \mathbf{x}_{\tau-m}^{(j)}; \mathbf{p}_{\tau}^{(j)}; w_{\tau}^{(j)} \right\} \quad (4)$$

$$j = 1, \dots, n$$

Weights are nonnegative and satisfy $\sum_{j=0}^1 w_{\tau}^{(j)} = 1$. The notation $\mathbf{p}_{\tau}^{(j)}$ indicates the outcome of \mathbf{P} for the j -th particle at time τ .

A Monte Carlo approximation of the posterior at time t is given by the empirical measure

$$\text{pdf}(\mathbf{x}_{\tau}, \mathbf{p} | \mathbf{y}_0, \dots, \mathbf{y}_{\tau}) \approx \sum_{j=1}^n w_{\tau}^{(j)} \delta(\mathbf{x}_{\tau} - \mathbf{x}_{\tau}^{(j)}) \delta(\mathbf{p} - \mathbf{p}_{\tau}^{(j)}) \quad (5)$$

where $\delta(\cdot)$ is the multi-dimensional Dirac delta function. We note that this measure is referred to as a PDF with an abuse of notation, since the Dirac delta function is not absolutely continuous with respect to the Lebesgue measure.

Figure 1 depicts the procedure for the recursive update of the particles, which consists of three steps:

Prediction prediction of the states is provided by their expected value at time $\tau+1$:

$$\tilde{\mathbf{x}}_{\tau+1}^{(j)} = \int_{\mathcal{I}_{\mathbf{X}}} \mathbf{x} q(\mathbf{x}, \mathbf{p}_{\tau}^{(j)} | \mathbf{y}_{\tau+1}, \mathbf{x}_{\tau}^{(j)}, \dots, \mathbf{x}_{\tau-m}^{(j)}) d\mathbf{x} \quad (6)$$

$$j = 1, \dots, n$$

Artificial evolution of the parameters using kernel smoothing consists of using a Gaussian mixture model (GMM) to

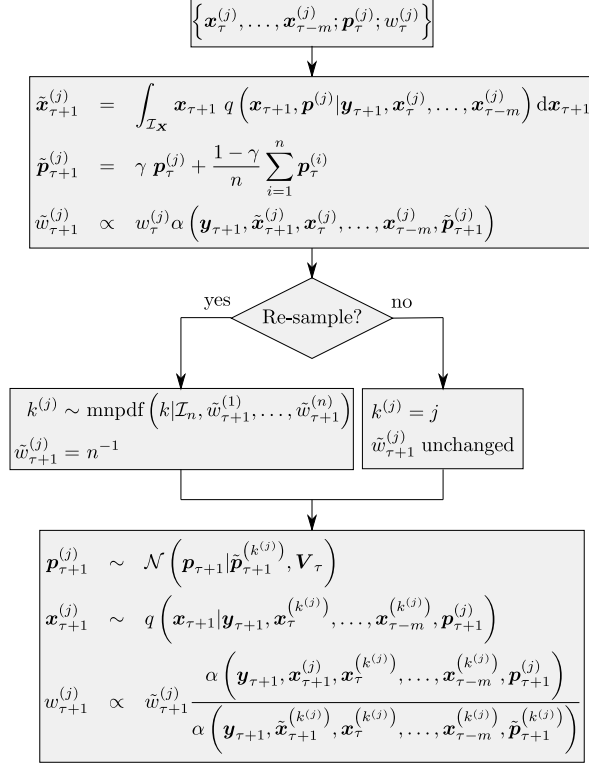


Fig. 1. Overview of the algorithm. At every time step, this loop is repeated for the n particles.

update $\mathbf{p}_\tau^{(j)}$ [17]. Prior update is given by the location of GMM's kernels,

$$\tilde{\mathbf{p}}_{\tau+1}^{(j)} = \gamma \mathbf{p}_\tau^{(j)} + \frac{1-\gamma}{n} \sum_{i=1}^n \mathbf{p}_\tau^{(i)}, \quad j = 1, \dots, n \quad (7)$$

where $\gamma \in [0, 1)$ is a discount factor for the dispersion of the variance of the parameters. Section 3.2 provides with further insight into this parameter.

The weights of the mixture's kernels are computed with the outcomes of Eqs. (6) and (7):

$$\tilde{w}_{\tau+1}^{(j)} \propto w_\tau^{(j)} \alpha(\mathbf{y}_{\tau+1}, \tilde{\mathbf{x}}_{\tau+1}^{(j)}, \mathbf{x}_\tau^{(j)}, \dots, \mathbf{x}_{\tau-m}^{(j)}, \tilde{\mathbf{p}}_{\tau+1}^{(j)}) \quad (8)$$

Here, the function α is defined as

$$\alpha(\mathbf{y}_{\tau+1}, \mathbf{x}_{\tau+1}, \mathbf{x}_\tau, \dots, \mathbf{x}_{\tau-m}, \mathbf{p}) = \frac{f(\mathbf{x}_{\tau+1} | \mathbf{x}_\tau, \dots, \mathbf{x}_{\tau-m}, \mathbf{p}) g(\mathbf{y}_{\tau+1} | \mathbf{x}_{\tau+1}, \mathbf{p})}{q(\mathbf{x}_{\tau+1}, \mathbf{p} | \mathbf{y}_{\tau+1}, \mathbf{x}_\tau, \dots, \mathbf{x}_{\tau-m})} \quad (9)$$

Re-sampling when multiple recursive updates are performed, weights might become unevenly distributed, with most of them approaching zero. When this happens, only one to very few particles efficiently contribute to the measure of Eq. (5), whose variance degenerates, and the posterior

distribution is not adequately approximated, whereas the memory to store a particle and the computations involved in its update are independent of the specific value of the weight. In other words, a huge effort is devoted to propagating particles with vanishing weights, whose contribution to Eq. (5) is negligible. This issue is referred to as *degeneracy*.

To prevent degeneracy from occurring, a new set of uniformly weighted particles is re-sampled from Eq. (5). This is achieved by sampling n integer coefficients, $k^{(j)}$ $j = 1, \dots, n$, with values in $\mathcal{I}_n = \{1, 2, \dots, n\}$ and corresponding probabilities $\{\tilde{w}_{\tau+1}^{(1)}, \tilde{w}_{\tau+1}^{(2)}, \dots, \tilde{w}_{\tau+1}^{(n)}\}$:

$$k^{(j)} \sim \text{mnpdf}(k | \mathcal{I}_n, w_{\tau+1}^{(1)}, \dots, w_{\tau+1}^{(n)}) \quad (10)$$

$$j = 1, \dots, n$$

Here, $\text{mnpdf}(\cdot | \mathcal{I}_n, w_{\tau+1}^{(1)}, \dots, w_{\tau+1}^{(n)})$ denotes the \mathcal{I}_n -valued multinomial distribution. After re-sampling, predicted weights are reset to $\tilde{w}_{\tau+1}^{(j)} = n^{-1}$, $j = 1, \dots, n$.

Several existing algorithms perform re-sampling at each time step. Because secular effects of non-gravitational forces need long observation windows to become appreciable, recursive updates are needed to identify good particles, i.e., good particles have to collect multiple 'good marks' before they can be distinguished from bad ones. For this reason, we discourage systematic re-sampling in this problem. Hence, we re-sample only if both of the following conditions are satisfied:

1. at least r time steps elapsed since the last re-sampling;
2. the degeneracy indicator, $\left[\sum_{j=1}^n (\tilde{w}_{\tau+1}^{(j)})^2 \right]^{-1}$, is below a prescribed threshold. We note that the indicator is in the range $[1, n]$ and it equals the two corner cases 1 and n either if all weights but one are equal to zero, or if particles are uniformly weighted, respectively.

If re-sampling does not occur, weights $\tilde{w}_{\tau+1}^{(j)}$ are not modified and $k^{(j)} = j \forall j \in [1, n]$.

Update all kernels of the GMM used for artificial evolution share the same variance,

$$\mathbf{V}_\tau = \frac{1-\gamma^2}{n-1} \sum_{j=1}^n (\mathbf{p}_\tau^{(j)} - \bar{\mathbf{p}}_\tau) (\mathbf{p}_\tau^{(j)} - \bar{\mathbf{p}}_\tau)^T \quad (11)$$

where $\bar{\mathbf{p}}_\tau = \frac{1}{n} \sum_{i=1}^n \mathbf{p}_\tau^{(i)}$. The coefficient $(1-\gamma^2)$ is introduced so that the unweighted mixture preserves both mean and variance of the sample $[\mathbf{p}_\tau^{(1)}, \mathbf{p}_\tau^{(2)}, \dots, \mathbf{p}_\tau^{(n)}]$.

Hence, states and parameters are updated by sampling from the GMM and importance distribution, respectively,

$$\mathbf{p}_{\tau+1}^{(j)} \sim \mathcal{N}\left(\mathbf{p}_{\tau+1} | \tilde{\mathbf{p}}_{\tau+1}^{(k^{(j)})}, \mathbf{V}_t\right) \quad (12)$$

$$\mathbf{x}_{\tau+1}^{(j)} \sim q\left(\mathbf{x}_{\tau+1} | \mathbf{y}_{\tau+1}, \mathbf{x}_{\tau}^{(k^{(j)})}, \dots, \mathbf{p}_{\tau+1}^{(j)}\right) \quad (13)$$

$$w_{\tau+1}^{(j)} \propto \tilde{w}_{\tau+1}^{(j)} \frac{\alpha\left(\mathbf{y}_{\tau+1}, \mathbf{x}_{\tau+1}^{(j)}, \mathbf{x}_{\tau}^{(k^{(j)})}, \dots, \mathbf{p}_{\tau+1}^{(j)}\right)}{\alpha\left(\mathbf{y}_{\tau+1}, \tilde{\mathbf{x}}_{\tau+1}^{(k^{(j)})}, \dots, \tilde{\mathbf{p}}_{\tau+1}^{(k^{(j)})}\right)} \quad (14)$$

for $j = 1, \dots, n$.

3. NON-GRAVITATIONAL FORCE ESTIMATION

After detailing the general algorithm in Section 2, we now apply it to non-gravitational force estimation: first, the various constituents of the filter are defined; second, the transitional, marginal likelihood, and proposal PDF are inferred by means of maximum likelihood estimation; finally, an insight into the choice of the filter parameters is provided. All forces are taken to be per mass unit in what follows.

Let Δt and t_{orb} be the (dimensional) time step of the filter and the orbital period, respectively. Denote by $\mathcal{E}_{\tau} \equiv \mathcal{E}(\tau \Delta t)$ the 6-dimensional set of orbital elements at time $\tau \Delta t$. Its averaged counterpart, $\bar{\mathcal{E}}_{\tau}$, is defined as

$$\bar{\mathcal{E}}_{\tau} = \frac{1}{t_{orb}} \int_{-t_{orb}/2}^{t_{orb}/2} \mathcal{E}(\tau \Delta t + t) dt \quad (15)$$

Noisy observations of the averaged orbital elements are available. Although advanced models for the measurement noise can be exploited, additive noise, Ξ_{τ} , is used in this work because it facilitates the inference of the PDF g . Thus, the measurement equation reads

$$\mathbf{Y}_{\tau} = \bar{\mathcal{E}}_{\tau} + \Xi_{\tau} \quad (16)$$

where the noise is such that $\Xi_{\tau} | \bar{\mathcal{E}}_{\tau} \sim g_{\bar{\mathcal{E}}}(\xi_{\tau} | \bar{\mathcal{E}}_{\tau})$ and $g_{\bar{\mathcal{E}}}(\xi_{\tau} | \bar{\mathcal{E}}_{\tau}) \equiv g(\bar{\mathcal{E}}_{\tau} + \xi_{\tau} | \mathbf{x}_{\tau})$. Typical means to gather measurements of averaged elements include either converting GPS data with a contact transformation or using TLE, which are available for most low-Earth orbit (LEO) objects. The former option is pursued in this paper, and a first-order Brouwer-Lyddane model is used [18]. Although the contact transformation is a noise source, exploiting averaged elements enhances the robustness for mis-modeling of high-degree gravitational harmonics. In addition, analytical and semi-analytical techniques can be naturally integrated into the algorithm to propagate particles.

Averaged elements constitute part of the state variables. In addition, the desired non-gravitational force, $\mathbf{f}^{(ng)}$, is also

included, so that

$$\mathbf{X}_{\tau} = \left\{ \begin{array}{l} \bar{\mathcal{E}}_{\tau} \\ \mathbf{f}_{\tau}^{(ng)} \end{array} \right\} \quad (17)$$

Let $\dot{\mathcal{E}}(\mathcal{E}, \mathbf{f})$ be the right-hand terms of the Gauss variational equations (GVE) for a prescribed set of osculating elements, \mathcal{E} , and a perturbing force, $\mathbf{f}(\mathcal{E}, t)$. In this work, we use equinoctial elements, whose definition and corresponding GVE are given in Appendix A. Averaging the GVE and integrating from time $\tau \Delta t$ to $(\tau + 1) \Delta t$ yields the averaged increment from $\bar{\mathcal{E}}_{\tau}$ to $\bar{\mathcal{E}}_{\tau+1}$,

$$\Delta \bar{\mathcal{E}}_{\tau} = \int_{\tau \Delta t}^{(\tau+1) \Delta t} \left(\frac{1}{t_{orb}} \int_{t-t_{orb}/2}^{t+t_{orb}/2} \dot{\mathcal{E}}(\mathcal{E}(s), \mathbf{f}(\mathcal{E}, s)) ds \right) dt \quad (18)$$

Because the GVE are linear in the perturbing force, the propagation of averaged elements can be recast as

$$\bar{\mathcal{E}}_{\tau+1} = \bar{\mathcal{E}}_{\tau} + \Delta \bar{\mathcal{E}}_{\tau}^{(g)} + \Delta \bar{\mathcal{E}}_{\tau}^{(ng)} + \Delta \bar{\mathcal{E}}_{\tau}^{(noise)} \quad (19)$$

where $\Delta \bar{\mathcal{E}}_{\tau}^{(g)}$, $\Delta \bar{\mathcal{E}}_{\tau}^{(ng)}$ denote the contributions to $\Delta \bar{\mathcal{E}}_{\tau}$ due to gravitational and non-gravitational perturbations, respectively; $\Delta \bar{\mathcal{E}}_{\tau}^{(noise)}$ includes effects of all remaining non-modeled forces, e.g., truncated gravitational harmonics, tides, and relativistic effects. The aforementioned underlying propagator defines which perturbations are included in $\Delta \bar{\mathcal{E}}_{\tau}^{(g)}$ and it approximates $(\Delta \bar{\mathcal{E}}_{\tau}^{(g)} + \Delta \bar{\mathcal{E}}_{\tau}^{(ng)})$. For the sake of conciseness, integration errors are not explicitly mentioned in Eq. (19), but they are automatically accounted for while estimating the HMM according to Section 3.1. The remaining perturbation $\Delta \bar{\mathcal{E}}_{\tau}^{(noise)}$ is modeled as an $\mathcal{I}_{\bar{\mathcal{E}}}$ -valued stochastic process distributed according to

$$\Delta \bar{\mathcal{E}}_{\tau}^{(noise)} | (\bar{\mathcal{E}}_{\tau}, \dots, \bar{\mathcal{E}}_{\tau-m}) \sim f_{\bar{\mathcal{E}}}(\xi_{\tau} | \bar{\mathcal{E}}_{\tau}, \dots, \bar{\mathcal{E}}_{\tau-m}) \quad (20)$$

Parametric models of the aerodynamic and SRP perturbations are used to propagate $\mathbf{f}_{\tau}^{(ng)}$:

$$\mathbf{f}_{\tau+1}^{(ng)} = \Lambda_{\tau}^T \left\{ \begin{array}{l} \mathbf{f}^{(drag)}(\bar{\mathcal{E}}_{\tau} + \Delta \bar{\mathcal{E}}_{\tau}, \mathbf{p}_{\tau}, (\tau + 1) \Delta t) \\ \mathbf{f}^{(srp)}(\bar{\mathcal{E}}_{\tau} + \Delta \bar{\mathcal{E}}_{\tau}, \mathbf{p}_{\tau}, (\tau + 1) \Delta t) \end{array} \right\} \quad (21)$$

$$\Lambda_{\tau} | (\mathbf{f}_{\tau}^{(ng)}, \dots, \mathbf{f}_{\tau-m}^{(ng)}, \mathbf{p}) \sim f_{\Lambda}(\lambda_{\tau} | \mathbf{f}_{\tau}^{(ng)}, \dots, \mathbf{f}_{\tau-m}^{(ng)}, \mathbf{p}) \quad (22)$$

Here, $\{\Lambda_{\tau} \in (\mathbb{R}^+)^2, \tau \in \mathbb{N}^+\}$ is an $(\mathbb{R}^+)^2$ -valued multiplicative noise modeling aleatory uncertainties, e.g., due to solar and geomagnetic activity or attitude of a tumbling de-

bris. In this work, $\mathbf{f}^{(drag)}$ and $\mathbf{f}^{(srp)}$ read

$$\mathbf{f}^{(drag)}(\bar{\mathcal{E}}, \mathbf{p}, t) = -\frac{1}{2}\rho(\bar{\mathcal{E}}, \mathbf{p}) C_b(\mathbf{p}, t) v_{tas} \mathbf{v}_{tas} \quad (23)$$

$$\mathbf{f}^{(srp)}(\bar{\mathcal{E}}, \mathbf{p}, t) = -P_{\odot} C_r(\mathbf{p}) \frac{S_{srp}(t)}{m} \frac{\mathbf{r}_{\odot}}{r_{\odot}^3} \delta_{eclipse} \quad (24)$$

where $\mathbf{v}_{tas}(\bar{\mathcal{E}})$, $\mathbf{r}(\bar{\mathcal{E}})$, m , S_{srp} , $P_{\odot}(t) = 4.56 \cdot 10^{-6} \text{ N/m}^2$, $\mathbf{r}_{\odot}(t)$, $\delta_{eclipse}$, and r_{eq} are the satellite's velocity with respect to the atmosphere, its position, mass, and cross-sectional area with respect to the Sun direction, the radiation pressure, the Sun position vector in astronomical units, a switch function which equals 1 if the satellite is in sunlight and 0 otherwise, and the mean equatorial radius, respectively; atmospheric density, ρ , ballistic coefficient, C_b , and reflectivity coefficient, C_r , are prescribed parametric models, e.g., exponential atmosphere or harmonic expansion as illustrated in the case study detailed in Section 4.2; temporal variations of C_b and S_{srp} are due to available information on attitude dynamics. Indeed, more advanced models can be used but the specific underlying propagator may limit their choice. This is further discussed in Section 4, where the performance of two propagators is compared.

Finally, the process noise due to $\Delta\bar{\mathcal{E}}_{\tau}$ and $\mathbf{\Lambda}_{\tau}$ can reasonably be assumed as statistically independent, yielding

$$f(\mathbf{x}_{\tau+1}(\xi_{\tau}, \lambda_{\tau}) | \mathbf{x}_{\tau}, \dots, \mathbf{x}_{\tau-m}, \mathbf{p}) \equiv f_{\bar{\mathcal{E}}}(\xi_{\tau} | \bar{\mathcal{E}}_{\tau}, \dots, \bar{\mathcal{E}}_{\tau-m}) f_{\Lambda}(\lambda_{\tau} | \mathbf{f}_{\tau}^{(ng)}, \dots, \mathbf{f}_{\tau-m}^{(ng)}, \mathbf{p}) \quad (25)$$

where $\mathbf{x}_{\tau+1}(\xi_{\tau}, \lambda_{\tau})$ denotes the outcome of $\mathbf{X}_{\tau+1}$ given the realizations ξ_{τ} and λ_{τ} of the processes defined in Eqs. (20) and (22), respectively.

3.1. Inference of the HMM via maximum likelihood estimation

Targeting practical implementation of the filter, a model of the importance distribution, q , and of the various PDF of the HMM, namely $g_{\bar{\mathcal{E}}}$, $f_{\bar{\mathcal{E}}}$, and f_{Λ} , is required. This can be achieved by means of maximum likelihood estimation, which involves selecting an adequate 'labeled' PDF, e.g., multivariate Gaussian or mixture model, followed by inferring suitable values to its parameters from available data.

Consider a set of n samples s_1, \dots, s_n of a random variable S and a PDF $p_S(s; \vartheta)$, where ϑ is the set of parameters defining the distribution, e.g., the mean and variance for a Gaussian distribution. According to the maximum likelihood method, these parameters are chosen such that they are consistent, e.g., positive definite covariance, and maximize the log-likelihood function

$$\mathcal{L}(\vartheta) = \sum_{j=1}^n \log(p_S(s_j | \vartheta)) \quad (26)$$

In this work, we use GMMs as labeled distributions. Hence, ϑ consist of the weights, means and variances of the kernels. GMMs provide flexibility in the representation of both marginal distributions and correlations. In addition, samples can be easily drawn from GMMs and their evaluation is straightforward.

The uncertainty characterization proposed in [19] is used to generate samples of the 'true' averaged elements. For this purpose, the outer and inner integrals of Eq. (18) are accurately evaluated by means of the Dormand-Prince method based on a 7-th order Runge-Kutta method followed by high-order Gauss quadrature, respectively.

3.2. Considerations for the choice of the filter parameters

A satisfactory trade-off between accurate and rapid convergence is achieved by carefully setting up the parameters of the filter. The first parameter to consider is the number of particles, n . Increasing n nearly-linearly increases the overall computational burden. However, there must be enough particles to adequately represent the posterior distribution and to delay degeneracy. This is particularly true during the early phase of the estimation, when uncertainty in the parameters \mathbf{p} is still very large. Adaptive choice of n is encouraged. This can be achieved during the re-sampling step.

Because of the aforementioned secular effects of non-gravitational perturbations, and because measurement are statistically independent of time, increasing the filter's time step, Δt , and re-sampling rate, r , enhances signal-to-noise ratio and, as such, improves the convergence of the estimation. Augmenting r is preferred when high-fidelity models of the non-gravitational force are used, because large time steps would reduce sensitivity to short-period variations. Nonetheless, degeneracy may occur for large r . Based on our experience, the product $r \Delta t$ should be of the order of one-to-few orbital periods.

Neglected gravitational harmonics are the major source of process noise for averaged orbital elements. The order of the HMM, $(m + 1)$, is a crucial parameter for mitigating their impact. Specifically, Earth's rotation causes relevant correlations in the time series of the noise after about one day. For example, Figure 2 depicts the autocorrelation of the process noise of the averaged orbital elements for the case study detailed in Section 4. Ideally, the order of the HMM should be large enough to cover this interval, but this may dramatically increase the required memory to store particles and augment the complexity of the importance and marginal prior distribution. Figure 2 also shows that all autocorrelations are close to one when the time step is below 10 minutes, so that we suggest using $m = 1$ if the filter's time step is of this order of magnitude. In this case, using $m = 0$ would result in extremely severe process noise, while larger m would be an unnecessary waste of computational resources.

Finally, the parameter γ regulates the memory of the par-

Table 1. Influence of the filter’s parameters on the quality of the estimation.

Parameter	Benefits when increased	Drawbacks when increased
n	Enhanced representation of the posterior Convergence when \mathbf{p} has large variance	Computational cost increases
Δt	Improved signal-to-noise ratio	Low sensitivity to short-period variations
r	Improved signal-to-noise ratio	Degeneracy might occur
m	Reduced sensitivity to process noise Enhanced convergence	Increased memory to store particles Increased complexity PDFs
γ	Enhanced identification of good particles	Diversity particles after multiple updates

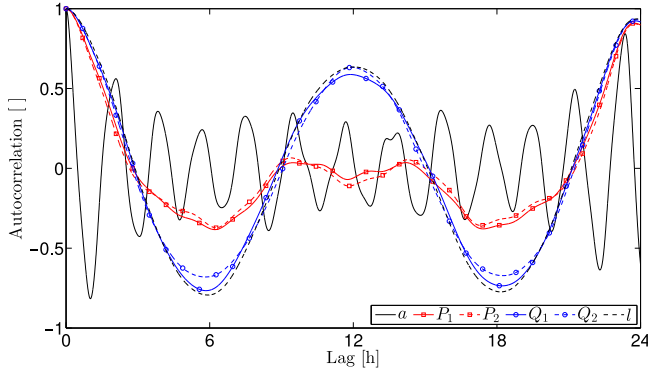


Fig. 2. Autocorrelation of the process noise of averaged elements using the analytical propagator. Here, a , P_1 , P_2 , Q_1 , Q_2 , and L denote the equinoctial elements defined in Appendix A.

ticles: according to Eqs. (7) and (11), the parameters \mathbf{p} are nearly unchanged after being updated if $\gamma \simeq 1$; on the contrary, they lose most memory of their previous value if $\gamma \simeq 0$. According to [17], values between 0.96 and 0.99 are reasonable for this parameter. We sustain this recommendation herein, owing to the need for multiple updates to identify ‘good’ particles.

Table 1 summarizes all these caveats.

4. NUMERICAL SIMULATIONS

Numerical simulations are carried out to assess the performance of the filter in a realistic scenario. The simulated environment includes gravitational harmonics up to order and degree 10, third-body perturbations of Sun and Moon, aerodynamic force, and SRP. The Sentman model is used to compute the aerodynamic force as a function of the geometric and ballistic properties of the satellite as described in [20]. Variable accommodation of the energy and thermal flow are assumed and the NRLMSISE-00 atmospheric model is used. A parallelepiped-shaped satellite is considered, and attitude is such that one geometrical axis points toward the orbital angular momentum vector whereas the pitch angle, which is defined as the angle between the orbital velocity and the normal to the smallest face of the parallelepiped, is imposed. Histor-

ical data of the solar activity are exploited to model the space weather.

Most of these perturbations are neglected by the underlying orbital propagator of the filter and are part of the process noise. Two different implementations of the filter’s propagator are considered herein:

Analytical this propagator is based on the analytical model proposed in [21], which assumes an oblate planet and uniform atmosphere, i.e., vertical rarefaction, day-night bulge and all other temporal and spatial variations of the atmospheric density are neglected. The low computational cost comes to the price of restrictions on the non-gravitational force model, which needs to be consistent with the aforementioned assumptions. Specifically, SRP is neglected, and only the averaged drag can be estimated. The ballistic coefficient is computed as

$$C_b(t) = \frac{C_d}{m} (S_d(t) + S_{d,0}) \quad (27)$$

where S_d and m are the cross sectional area and the mass of the satellite, respectively. The vector of parameters is $\mathbf{p} = [C_d, S_{d,0}]^T$, where C_d is the drag coefficient, and $S_{d,0}$ is a constant area aimed at approximating the effects of thermal flow, which are such that long-shaped satellites flying as an arrow experience larger drag than compact-shaped satellites for a given cross sectional area to mass ratio.

Numerical this propagator lies on the other side of the spectrum and consists of brute force integration of Eq. (6), which enables extreme flexibility. Hence, 20-th order Gauss quadrature and trapezoidal rule are used to compute the inner and outer integrals, respectively. The term $\Delta \bar{\mathcal{E}}_\tau^{(g)}$ includes gravitational harmonics up to order and degree 4 and third-body perturbations of Sun and Moon. Both SRP and instantaneous atmospheric force are estimated. For this purpose, the atmospheric density is expanded in Fourier series to account for near-periodic variations due to orbital eccentricity, atmospheric bulge, and Earth’s oblateness:

$$\rho = \rho_0 \left[1 + \sum_{j=1}^{n_{exp}} (c_j \cos(j L) + s_j \sin(j L)) \right] \quad (28)$$

Table 2. Parameters of the simulations. The acronyms (AP) and (NP) are used when different values of the parameters are used for the filter using the analytical and numerical propagator, respectively.

	Value
Initial orbital elements	
Semi-major axis	6828.137 km
Eccentricity	10^{-3}
Inclination	98 deg
Argument of perigee	120 deg
Right ascension of the ascending node	30 deg
True anomaly	15 deg
Epoch	1/4/2012
Ballistic properties	
Mass	3 kg
Size	$0.3 \text{ m} \times 0.1 \text{ m} \times 0.1 \text{ m}$
Pitch	$0.35\pi \frac{t}{t_{orb}}$
Filter parameters	
Number of particles, n	$\in [100, 3000]$
Filter's time step, Δt	60 min (AP) 3 min (NP)
Re-sampling rate, r	$\text{ceil}\left(\frac{t_{orb}}{\Delta t}\right)$
HMM order, m	3 (AP) 1 (NP)
Discount factor, γ	0.99
Number of kernels of the GMM	5

where c_j , s_j , n_{exp} , and L denote the coefficients and order of the expansion, and the true longitude defined in Appendix A, respectively. The vector of parameters is thus

$$\mathbf{p} = [C_d, S_{d,0}, c_1, s_1, \dots, c_{n_{exp}}, s_{n_{exp}}, C_r]^T.$$

Appending ρ_0 to \mathbf{p} is useless because ρ_0 is systematically multiplied by C_d . Choosing an arbitrary ρ_0 in the filter may shift the values of C_d , but it does not affect the error in the atmospheric force. For long-term scenarios, an exponential term has to be introduced in Eq. (28) to account for the vertical rarefaction due to orbital decay.

The simulation setup is detailed in Table 2. The number of samples is adapted during the re-sampling step. Specifically, n is reduced by 1% whenever at least 100 distinct coefficients $k^{(j)}$ are extracted from the multinomial distribution. On the contrary, n is increased by 5% when this condition is not satisfied. When the numerical propagator is used, the expansion of the Fourier series of the atmospheric density is truncated at the second term, i.e., $n_{exp} = 2$.

Measurement noise is mainly due to the first-order Brouwer-Lyddane contact transformation [18]. In addition, GPS noise is modeled as non-correlated white noise with standard deviation equal to 5 m and 2 cm/s for the position and velocity components, respectively. This modeling of the GPS noise is not realistic and colored noise should be considered instead. Nonetheless, the contribution of GPS noise is negligible compared to the noise introduced by the contact transformation.

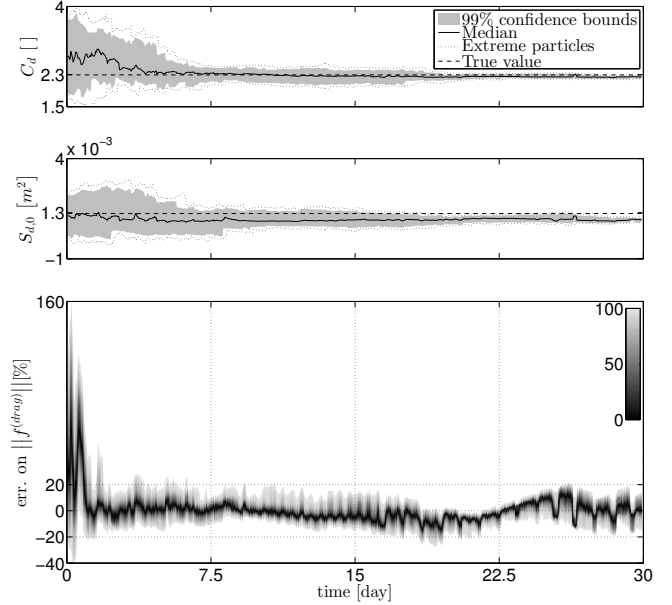


Fig. 3. Filter based on the analytical propagator. Convergence of the parameters, \mathbf{P} , and error in the averaged aerodynamic force. Shades of grey in the bottom figure denote the confidence level.

4.1. Filter with analytical propagator

Figure 3 depicts the convergence of the parameters and the error in the averaged drag when the filter based on the analytical propagator is used. Very broad and biased initial PDFs of the parameters are deliberately exploited to emphasize the robustness of the algorithm. Specifically, we used

$$\mathbf{p}_0 \sim \mathcal{U} \left(\begin{bmatrix} 0.8C_d^{(true)} \\ 0.1S_{d,0}^{(true)} \end{bmatrix}, \begin{bmatrix} 1.6C_d^{(true)} \\ 1.7S_{d,0}^{(true)} \end{bmatrix} \right) \quad (29)$$

where $C_d^{(true)} \simeq 2.3$ and $S_{d,0}^{(true)} \simeq 13 \text{ cm}^2$ are the true averaged values of the parameters C_d and $S_{d,0}$, and $\mathcal{U}(a, b)$ denotes the multivariate uniform distribution with lower and upper bounds a and b , respectively. Dotted curves denote the envelope of the particles, while shaded regions outline 99% confidence bounds deduced by the empirical measure of Eq. (5). After re-sampling, the envelope is narrowed down to gather particles close to the high-confidence region.

The median of the relative residual bias of $S_{d,0}$ is significantly greater than the one of C_d , because its contribution to the ballistic coefficient is less important compared to C_d .

Regardless the aforementioned broad initial PDF of the parameters and the low frequency rate of the measurements, i.e., $\Delta t = 1$ hour, the estimation of the averaged aerodynamic force converges below 20% error in about three days. We believe that this is a significant result given the modest data used by the filter.

The error is unsteady because of solar activity, which is

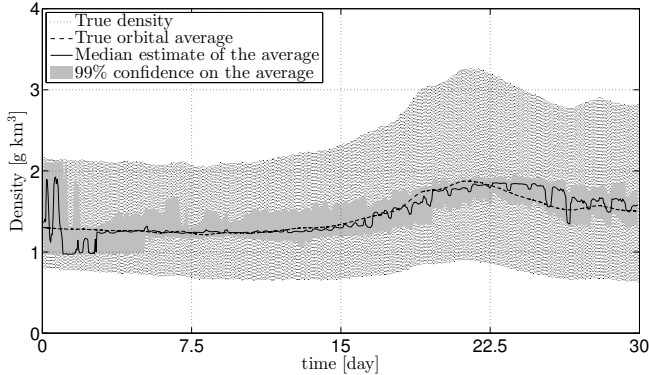


Fig. 4. Filter based on the analytical propagator. Dotted and dashed curves denote atmospheric density and its orbital average, respectively. The solid line and the shaded region are the median and 99% confidence bounds of the estimation of $\Lambda_{\tau,1}$, respectively.

a stochastic process in nature. For this reason, its impact on the uncertainty in the aerodynamic force cannot be mitigated without using other data than satellite state observations. Figure 4 shows the evolution of the averaged drag, which varies up to 50% during the simulation. The trend is captured within the 99% confidence bounds of the estimation, but these bounds remain relatively large in time. Enhanced performance can be achieved by providing information on some space weather proxies to the filter and by correlating them with Λ .

The current scenario uses the least computationally demanding filter among the proposed ones, so that we wish to briefly comment on the possibility to implement the algorithm on-board. Because the filter’s time step can be rather large, the computational time to accomplish one iteration is not critical even for low-end micro-controllers. Available memory is the main issue. On top of the memory required to store and evaluate the PDFs of the model and to perform basic algebraic operations, two sets of particles need to be held in memory. Recalling that one particle is defined according to Eq. (4) and assuming double-precision variables, the memory required to store two particle sets is

$$2 n [m \dim(\mathbf{X}) + \dim(\mathbf{P}) + 1] 8 \text{ B} \quad (30)$$

where 8 B is the size of one double-precision variable. This number can be reduced by noting that $m - 1$ past states are shared by the two sets, but we consider the conservative value of Eq. (30) in the context of this gross estimation. Figure 5 illustrates the number of samples used during the simulation. Once the estimation is sufficiently converged, the filter uses less than 500 samples in average, which correspond to 192 kB according to Eq. (30). With these caveats in mind, the algorithm should be reasonably implementable on micro-controllers with 512kB memory.

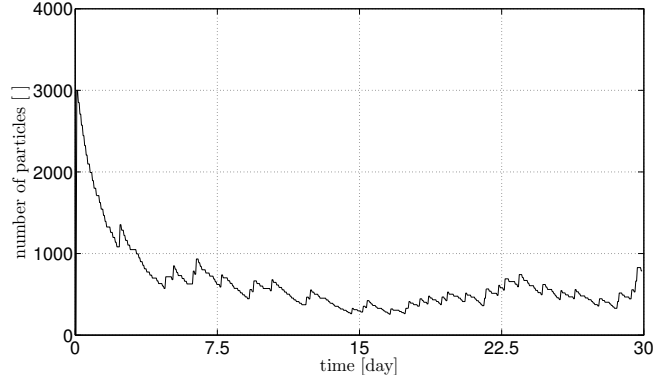


Fig. 5. Filter based on the analytical propagator. Number of samples as a function of time.

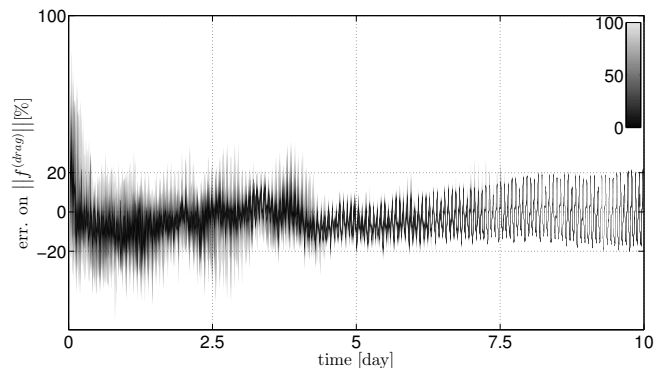


Fig. 6. Filter based on the numerical propagator. Error in the instantaneous aerodynamic force. Shades of grey denote the confidence level.

4.2. Filter with numerical propagator

The filter of this case study uses numerical integration to propagate particles, which enables the possibility to compute both the instantaneous aerodynamic and SRP forces. Uniform uncertainty of $\pm 20\%$ on all coefficients of the series expansion of Eq. (28) is used at the initial step, whereas the same distribution of Eq. (29) is used for C_d and $S_{d,0}$.

Convergence of the error in the aerodynamic force is illustrated in Figure 6. Similarly to the previous case study, the error is confined to $\pm 20\%$ after about 5 days. However, this result outperforms the previous one, because the instantaneous force is now estimated, which exhibits variations of one order of magnitude due to orbital eccentricity, day-night atmospheric variations, and Earth’s oblateness. Figure 7 shows that these variations are adequately captured by the filter.

Finally, the convergence of the reflectivity coefficient is depicted in Figure 8. Compared to the aerodynamic force, the estimation of this parameter is less striking because of the low altitude, so that the SRP has minor impact on the evolution of the averaged elements and, consequently, on the particles

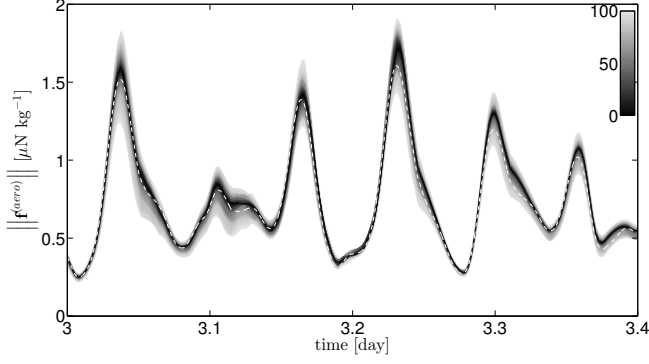


Fig. 7. Filter based on the numerical propagator. True and estimated aerodynamic force. The white-dashed line represents the norm of the true aerodynamic force. Shades of grey denote the confidence level of the estimation.

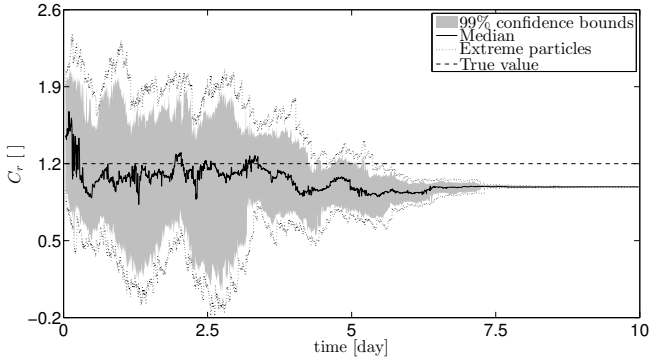


Fig. 8. Filter based on the numerical propagator. True and estimated reflectivity coefficient.

weights. Nonetheless, the reflectivity coefficient is estimated with less than a 20% precision, which is not completely depreciable considering that the algorithm ignores the physical bounds of C_r .

5. CONCLUSIONS

The filter proposed herein does not require in-situ accelerometers. Sequential measurements of mean orbital elements are processed instead. Secular effects of non-gravitational perturbations allow good particles to be identified after a sufficient training period even when coarse and arguably sporadic measurements are used.

High-fidelity numerical simulations show that both the aerodynamic force and the SRP can be estimated within 20% error using a first-order contact transformation and no information on the actual solar activity. This result is strongly dependent on the specific underlying orbital propagator, which has to be chosen according to the available computational resources. However, the methodology is presented in a general framework, which can be straightforwardly adapted to any de-

sired propagator ranging from numerical brute-force integration to semi-analytical or analytical techniques.

A. GVE FOR EQUINOCTIAL ELEMENTS

Let $a, e, i, \omega, \Omega, f$, be the classical orbital elements, namely the semi-major axis, the eccentricity, the orbital inclination, the argument of perigee, the right ascension of the ascending node and the true anomaly, respectively. Equinoctial elements are defined as [22]

$$\mathcal{E} = (a, P_1, P_2, Q_1, Q_2, L)^T$$

where $L = \omega + \Omega + f$ is referred to as true longitude, and

$$\begin{aligned} P_1 &= e \sin(\omega + \Omega) & P_2 &= e \cos(\omega + \Omega) \\ Q_1 &= \tan \frac{i}{2} \sin \Omega & Q_2 &= \tan \frac{i}{2} \cos \Omega \end{aligned}$$

The GVE for the equinoctial elements are [22]

$$\begin{aligned} \dot{a} &= \frac{2a^2}{h} \left[(P_2 \sin L - P_1 \cos L) f_{p,r} + \frac{p}{r} f_{p,t} \right] \\ \dot{P}_1 &= \frac{r}{h} \left[-\frac{p}{r} \cos L f_{p,r} + \left(P_1 + \left(1 + \frac{p}{r} \right) \sin L \right) f_{p,t} \right. \\ &\quad \left. - P_2 (Q_1 \cos L - Q_2 \sin L) f_{p,h} \right] \\ \dot{P}_2 &= \frac{r}{h} \left[\frac{p}{r} \sin L f_{p,r} + \left(P_2 + \left(1 + \frac{p}{r} \right) \cos L \right) f_{p,t} \right. \\ &\quad \left. + P_1 (Q_1 \cos L - Q_2 \sin L) f_{p,h} \right] \\ \dot{Q}_1 &= \frac{r}{2h} (1 + Q_1^2 + Q_2^2) \sin L f_{p,h} \\ \dot{Q}_2 &= \frac{r}{2h} (1 + Q_1^2 + Q_2^2) \cos L f_{p,h} \\ \dot{L} &= \frac{h}{r^2} - \frac{r}{h} (Q_1 \cos L - Q_2 \sin L) f_{p,h} \end{aligned}$$

where $p, r, h, f_{p,r}, f_{p,t}$, and $f_{p,h}$ are the semi-latus rectum, the magnitude of the position vector and angular momentum, and the components of the specific perturbing force in the local-vertical-local-horizontal frame, respectively.

Acknowledgements

This work was partially supported by the Belgian National Fund for Scientific Research (FNRS) and by the European Research Council Starting Independent Researcher Grant 278231: Flight Algorithms for Disaggregated Space Architectures (FADER).

B. REFERENCES

- [1] V. M. Gotlib, E. N. Evlanov, B. V. Zubkov, V. M. Linkin, A. B. Manukin, S. N. Podkolzin, and V. I. Rebrov, "High-sensitivity quartz accelerometer for measurements of small accelerations of spacecraft," *Cosmic Research*, vol. 42, no. 1, pp. 54–59, Jan. 2004.

- [2] Byron D. Tapley, Bob E. Schutz, and George H. Born, "Fundamentals of orbit determination," *Statistical Orbit Determination*, p. 159–284, 2004.
- [3] B. D. Tapley, A. R. Neto, and B. E. Schutz, "Orbit determination in the presence of atmospheric drag errors," *Satellite Dynamics*, p. 154–169, 1975.
- [4] C. B. Winn, "Optimal estimation of unmodeled accelerations on the ONERA navigational satellite," *Journal of Spacecraft and Rockets*, vol. 12, no. 2, pp. 79–82, Feb. 1975.
- [5] Jason Zhang, Kefei Zhang, Ron Grenfell, and Rod Deakin, "GPS satellite velocity and acceleration determination using the broadcast ephemeris," *Journal of Navigation*, vol. 59, no. 2, pp. 293, Apr. 2006.
- [6] Bruce R Bowman and Kenneth Moe, "Drag coefficient variability at 175–500 km from the orbit decay analyses of spheres," in *Advances in the Astronautical Sciences*, 2005, vol. 123, pp. 117–136.
- [7] Arrun Saunders, Graham G. Swinerd, and Hugh G. Lewis, "Deriving accurate satellite ballistic coefficients from two-line element data," *Journal of Spacecraft and Rockets*, vol. 49, no. 1, pp. 175–184, Jan. 2012.
- [8] Daniel P. Lubey and Daniel J. Scheeres, "Identifying and estimating mismodeled dynamics via optimal control policies and distance metrics," *Journal of Guidance, Control, and Dynamics*, vol. 37, no. 5, pp. 1512–1523, Sep. 2014.
- [9] Arnaud Doucet, Simon Godsill, and Christophe Andrieu, "On sequential monte carlo sampling methods for bayesian filtering," *Statistics and computing*, vol. 10, no. 3, pp. 197–208, 2000.
- [10] Arnaud Doucet, Nando Freitas, and Neil Gordon, Eds., *Sequential Monte Carlo Methods in Practice*, Springer Science + Business Media, 2001.
- [11] James S. McCabe and Kyle J. DeMars, "Particle filter methods for space object tracking," in *AIAA/AAS Astrodynamics Specialist Conference*. Aug. 2014, number AIAA 2014-4308, American Institute of Aeronautics and Astronautics (AIAA).
- [12] Young Rok Kim, Sang-Young Park, Chandeok Park, Eun-Seo Park, and Hyung-Chul Lim, "Precise orbit determination with satellite laser ranging observations using a batch filter based on particle filtering," in *AIAA/AAS Astrodynamics Specialist Conference*. Aug. 2012, number AIAA 2012-5064, American Institute of Aeronautics and Astronautics (AIAA).
- [13] Alinda Mashiku, James Garrison, and J. Russell Carpenter, "Statistical orbit determination using the particle filter for incorporating non-gaussian uncertainties.," in *AIAA/AAS Astrodynamics Specialist Conference*. Aug. 2012, number AIAA 2012-5063, American Institute of Aeronautics and Astronautics (AIAA).
- [14] Guoqiang Zeng, Min Hu, and Hong Yao, "Relative orbit estimation and formation keeping control of satellite formations in low earth orbits," *Acta Astronautica*, vol. 76, pp. 164–175, July 2012.
- [15] Soon Sik Hwang and Jason L. Speyer, "Particle filters with adaptive resampling technique applied to relative positioning using GPS carrier-phase measurements," *IEEE Transactions on Control Systems Technology*, vol. 19, no. 6, pp. 1384–1396, Nov. 2011.
- [16] F. Daum, "Nonlinear filters: beyond the kalman filter," *IEEE Aerospace and Electronic Systems Magazine*, vol. 20, no. 8, pp. 57–69, Aug. 2005.
- [17] Jane Liu and Mike West, "Combined parameter and state estimation in simulation-based filtering," in *Sequential Monte Carlo Methods in Practice*, pp. 197–223. Springer Science + Business Media, 2001.
- [18] R. H. Lyddane, "Small eccentricities or inclinations in the Brouwer theory of the artificial satellite," *The Astronomical Journal*, vol. 68, pp. 555 – 558, Oct. 1963.
- [19] Lamberto Dell’Elce, Maarten Arnst, and Gaëtan Kerschen, "Probabilistic assessment of the lifetime of low-earth-orbit spacecraft: Uncertainty characterization," *Journal of Guidance, Control, and Dynamics*, vol. 38, no. 5, pp. 900–912, May 2015.
- [20] Eelco Doornbos, *Thermospheric Density and Wind Determination from Satellite Dynamics*, Springer Berlin Heidelberg, 2012.
- [21] Vladimir Martinusi, Lamberto Dell’Elce, and Gaëtan Kerschen, "Analytic propagation of near-circular satellite orbits in the atmosphere of an oblate planet," *Celestial Mechanics and Dynamical Astronomy*, vol. 123, no. 1, pp. 85–103, June 2015.
- [22] Richard H. Battin, *An Introduction to the Mathematics and Methods of Astrodynamics, Revised Edition*, American Institute of Aeronautics and Astronautics (AIAA), jan 1999.